Compact Electrothermal Reliability Modeling and Experimental Characterization of Bipolar Latchup in SiC and CoolMOS Power MOSFETs

Roozbeh Bonyadi, *Student Member, IEEE*, Olayiwola Alatise, *Member, IEEE*, Saeed Jahdi, *Student Member, IEEE*, Ji Hu, *Student Member, IEEE*, Jose Angel Ortiz Gonzalez, Li Ran, *Senior Member, IEEE*, and Philip A. Mawby, *Senior Member, IEEE*

***Abstract*—In this paper, a compact dynamic and fully coupled electrothermal model for parasitic BJT latchup is presented and validated by measurements. The model can be used to enhance the reliability of the latest generation of commercially available power devices. BJT latchup can be triggered by body-diode reverse-recovery hard commutation with high *dV/dt* or from avalanche conduction during unclamped inductive switching. In the case of body-diode reverse recovery, the base current that initiates BJT latchup is calculated from the solution of the ambipolar diffusion equation describing the minority carrier distribution in the antiparallel p-i-n body diode. For hard commutation with high *dV/dt*, the displacement current of the drain-body charging capacitance is critical for BJT latchup, whereas for avalanche conduction, the base current is calculated from impact ionization. The parasitic BJT is implemented in Simulink using the Ebers–Moll model and the temperature is calculated using a thermal network matched to the transient thermal impedance characteristic of the devices. This model has been applied to CoolMOS and SiC MOSFETs. Measurements show that the model correctly predicts BJT latchup during reverse recovery as a function of forward-current density and temperature. The model presented, when calibrated correctly by device manufacturers and applications engineers, is capable of benchmarking the robustness of power MOSFETs.**

***Index Terms*—Body diode, compact electrothermal modeling, inverter, MOSFET, p-i-n diodes, parasitic BJT latchup, SiC MOSFET reliability.**

I. Introduction

BODY diodes can sometimes be used as the antiparallel diodes in power MOSFET circuits. Because of the voltage blocking drift layer between the p-body and the drain, the body diode is effectively a p-i-n diode. Power MOSFET body diodes can be used in applications, such as dc–dc buck converters, bridge topology switching circuits, and high-performance PV converter cell, and can also be employed in synchronous rectified brushless DC motor drive inverter circuits [1]–[6]. In such applications, diode snappiness and high reverse recovery charge of the body diode can impose a significant amount of electrical stress and power loss on the MOSFETs [7]. The large reverse recovery charge is the result of an excessive amount of carriers stored in the charge storage region (drift layer) of the diode. Conventional lifetime control techniques (gold or platinum doping as well as irradiation) are not applicable in reducing the carrier lifetime as is the case with discrete diodes; hence, the body diode of the MOSFET can suffer from significant reverse charge. One of the main concerns regarding the usage of the body diode of power MOSFETs is the robustness of the device under hard commutation, e.g., in synchronous rectification, or in other circuits such as motor drives or primary-side switching of switch-mode power supplies [8], [9].

The high demand for high-frequency and efficient power converters has triggered research into SiC devices including power MOSFETs [10]. SiC MOSFETs are more suitable for high-voltage and high-speed applications due to their higher breakdown voltage, lower on-state resistance, and faster switching. SiC has a significantly smaller minority carrier lifetime, and as a result of the higher critical field, the thickness of the voltage blocking drift layer is approximately ten times less than silicon devices. Consequently, they show smaller reverse recovery with a higher breakdown voltage. The effect of using SiC MOSFET in synchronous rectification was studied in [2], which shows that the reverse recovery of SiC body diode was negligible as well as an improvement in the switching speed of the MOSFET. MOSFETs have parasitic n-p-n BJTs that can latchup under the right conditions, i.e., when the emitter–base voltage is forward biased, the base–collector voltage is reverse biased, and there is sufficient body current in the base [11], [12]. For the BJTs to latch, there must be a body current sufficient to cause a voltage drop greater than the emitter–base junction voltage of the parasitic BJT. To prevent this from happening, the source is usually grounded to the body by a high dose body implant and a common metal contact. However, at high temperatures, a nonzero body resistance and a nonzero body current can cause BJT latchup. The high *dV/dt* of the body diode during reverse recovery coupled with the parasitic drain-to-body capacitance within the MOSFET can cause a body current (*CdV/dt*) sufficient to latch the parasitic BJT. This is particularly pertinent to SiC MOSFETs where *dV/dt* is high, the minority carrier lifetime is low, and the body diode is snappy.

Manuscript received May 13, 2014; revised August 18, 2014 and October 27, 2014; accepted December 20, 2014. Date of publication January 7, 2015; date of current version August 21, 2015. This work was supported by EPSRC funding in collaboration with Jaguar Land Rover Automotive PLC and EPSRC funding through the underpinning power electronics devices theme research project (EP/L007010/1) and the components theme research project (EP/K034804/1). Recommended for publication by Associate Editor K. Sheng.

The authors are with the School of Engineering, University of Warwick, Coventry CV4 7AL, U.K. (e-mail: R.Bonyadi@warwick.ac.uk; O.Alatise@warwick.ac.uk; S.Jahdi@warwick.ac.uk; J.Hu@warwick.ac.uk; J.A.Ortiz-Gonzalez@warwick.ac.uk; L.Ran@warwick.ac.uk; P.A.Mawby@warwick.ac.uk).

Color versions of one or more of the figures in this paper are available online at http://ieeexplore.ieee.org.

Digital Object Identifier 10.1109/TPEL.2015.2388512

CoolMOS devices use the principle of the superjunction to achieve high blocking voltages while delivering low conduction losses. The alternate n and p columns in the drift region means that the body diode is not a conventional p-i-n diode and will, therefore, exhibit a different reverse recovery characteristic. In this paper, the reliability of the SiC MOSFET and CoolMOS body diode under reverse recovery is investigated experimentally and by modeling. The body diode of the MOSFET has been modeled using the Fourier series solution to the ambipolar diffusion equation (ADE). This is coupled with the electrothermal model of the parasitic BJT and is used as a compact physics-based electrothermal model for a SiC MOSFET and Si-based CoolMOS device. The impact of the temperature as well as current density on the diode recovery characteristics and failure mechanism of the MOSFET is investigated by the model and compared with experimental measurements. The proposed model can be used to investigate the conditions of device failure during purposeful or inadvertent reverse recovery of device body diode. The model is useful for estimating the reliability performance and giving deeper physical insight to the nature of bipolar latchup. Section II describes the development of the Fourier series model for the body diode, Section III describes the BJT electrothermal model, and Section IV discusses the results, while Section V concludes the paper.

II. Body Diode Model Development

There have been several publications that have detailed how the minority carrier distribution profile in the drift region can be modeled using the Fourier series solution to the ADE [9], [13]–[24]. The reverse recovery characteristics of the p-i-n body diode in this paper have been modeled using the same techniques developed for discrete p-i-n diodes. The ADE can also be solved using the finite-difference and finite-volume techniques; however, the Fourier series is the most computationally inexpensive way of solving it without too much loss of accuracy. The model takes conductivity modulation, Shockley–Read–Hall recombination, Auger recombination, carrier–carrier scattering, drift, diffusion, and displacement currents, depletion layers behavior, and local lifetime into account. Moreover, the model calculates the drift region voltage drop based on the conductivity modulation in the drift region. The ADE models the concentration of carriers in the drift region which determines the behavior of the device during the reverse recovery and is reconstructed using Fourier series in one dimension [19], [20]. In case of the CoolMOS model, it has been assumed that there is negligible carrier concentration gradient or electric field gradient across the lateral cross section of the device in comparison to the vertical cross section of the device. As a result, electrons flow from the cathode (the drain of the MOSFET) into the drift regions and holes flow from the anode (the p-body of the MOSFET) into the drift regions. Based on this, the 1-D solution of the Fourier series is applicable because of the assumption that the vertical concentration gradients are much higher than the lateral concentration gradients.

The model has been developed for a discrete p-i-n diode initially and, in this paper, has been extended to body diodes for SiC MOSFETs and CoolMOS devices.

Conductivity modulation in the drift region is the mechanism through which low conduction losses are enabled in p-i-n diodes and depends on minority carrier injection into the drift region. If the number of injected holes to the drift region becomes much greater than the background doping of the drift region, charge neutrality requires that the concentration of electrons and holes be equal to each other in that region: $p(x) = n(x)$. Using the continuity equations for the intrinsic region, we have

$$\frac{\partial n}{\partial t} = -\frac{n}{\tau_{HL}} + D_n \frac{\partial^2 n}{\partial x^2} + \mu_n \frac{\partial}{\partial x}(nE) \tag{1}$$

$$\frac{\partial p}{\partial t} = -\frac{p}{\tau_{HL}} + D_p \frac{\partial^2 p}{\partial x^2} + \mu_p \frac{\partial}{\partial x}(pE) \tag{2}$$

where, τ_{HL} is the high-level lifetime in the drift region (in order of 1 μs for silicon devices and 0.1 ns for SiC), and D_n (for Silicon 36.1798 cm^2/s and 34.3708 cm^2/s for SiC at room temperature) and D_p (11.6292 cm^2/s for Silicon and 2.3258 cm^2/s for SiC at room temperature) are the diffusion coefficients for electron and holes, respectively. Diffusion coefficients in SiC are smaller in comparison with silicon. Using charge neutrality equation and the continuity equations, the ADE is

$$\frac{\partial p(x,t)}{\partial t} = -\frac{p(x,t)}{\tau_{HL}} + \left(\frac{2\mu_n \mu_p V_T}{\mu_n + \mu_p}\right) \frac{\partial^2 p(x,t)}{\partial x^2}. \tag{3}$$

Diffusivity in ADE is calculated using the Einstein relationship ($D = \frac{kT}{q}\mu_n$, where k is the Boltzmann constant 1.38×10^{-23} J $\cdot$ K^{-1} and q is the electron charge 1.602×10^{-19} C) as follows:

$$D = \frac{2\mu_n \mu_p V_T}{\mu_n + \mu_p} = \frac{2 D_n D_p}{D_n + D_p}. \tag{4}$$

The ambipolar diffusion length is the length that shows how far electrons and holes can diffuse into the drift region before they recombine and it is $L_a = \sqrt{D\tau_{\mathrm{HL}}}$. This determines the shape of the catenary in the drift region. The ADE models the concentration of carriers in the drift region, which determines the behavior of the device during the reverse recovery. Each term of the ADE in (3) is multiplied by $\cos\left(\frac{\pi k(x-x_1)}{x_2-x_1}\right)$ and then integrated with respect to x_1 and x_2, which are the edges of the depletion region in the drift region from p side and n side, respectively

$$\begin{aligned} \text{Term 1} &= \int_{x_1}^{x_2} \frac{\partial p(x,t)}{\partial t} \cos\left(\frac{\pi k(x-x_1)}{x_2-x_1}\right) dx \\ &= \sum_{\substack{n=1 \\ n\neq k}}^{\infty} \frac{n^2 p_n}{n^2-k^2} \left[\frac{dx_1}{dt} - (-1)^{n+k}\frac{dx_2}{dt}\right] \\ &\quad + \frac{x_2-x_1}{2}\frac{dp_k}{dt} + \frac{p_k}{4}\left[\frac{dx_1}{dt} - \frac{dx_2}{dt}\right] \end{aligned} \tag{5}$$

$$\begin{aligned} \text{Term 2} &= \int_{x_1}^{x_2} \frac{p(x,t)}{\tau_{\mathrm{HL}}} \cos\left(\frac{\pi k(x-x_1)}{x_2-x_1}\right) dx \\ &= \frac{x_2-x_1}{2} p_k(t) \end{aligned} \tag{6}$$

$$\begin{aligned}\text{Term 3} &= D\int_{x_1}^{x_2} \frac{\partial^2 p(x,t)}{\partial x^2} \cos\left(\frac{\pi k(x-x_1)}{x_2-x_1}\right) dx \\ &= D\left[\left.\frac{\partial p(x,t)}{\partial x}\right|_{x_2} (-1)^k - \left.\frac{\partial p(x,t)}{\partial x}\right|_{x_1}\right] \\ &\quad - D\left(\frac{\pi k}{x_2-x_1}\right)^2 \frac{x_2-x_1}{2} p_k(t) \end{aligned} \tag{7}$$

where $p_k(t)$ are the Fourier series coefficients. Putting these three terms in the ADE, i.e., (3), gives the reconstruction of the ADE using Fourier series [19], [20]

$$\begin{aligned} p(x,t) &= \sum\nolimits_{k=0}^{\infty} p_k(t) \cos\left(\frac{\pi k(x-x_1)}{x_2-x_1}\right) \\ k &> 0: \\ \frac{dp_k}{dt} &= \frac{2D}{x_2-x_1}\left[\left.\frac{\partial p}{\partial x}\right|_{x_2}(-1)^k - \left.\frac{\partial p}{\partial x}\right|_{x_1}\right] \\ &\quad - p_k\left(\frac{1}{\tau_{\mathrm{HL}}} + \frac{D\pi^2k^2}{(x_2-x_1)^2}\right) \\ &\quad - \frac{2}{(x_2-x_1)}\left(\sum_{\substack{n=1\\n\neq k}}^{\infty} \frac{n^2 p_n}{n^2-k^2}\frac{dx_1}{dt} - (-1)^{n+k}\frac{dx_2}{dt}\right) \\ &\quad - \frac{p_k}{2(x_2-x_1)}\left(\frac{dx_1}{dt} - \frac{dx_2}{dt}\right) \\ k &= 0: \\ \frac{dp_0}{dt} &= \frac{D}{x_2-x_1}\left[\left.\frac{\partial p}{\partial x}\right|_{x_2} - \left.\frac{\partial p}{\partial x}\right|_{x_1}\right] - \frac{p_0}{\tau_{HL}} \\ &\quad - \frac{1}{(x_2-x_1)}\sum_{n=1}^{\infty} p_n\left(\frac{dx_1}{dt} - (-1)^n\frac{dx_2}{dt}\right). \end{aligned} \tag{8}$$

The boundary conditions of the equation above (x_1 and x_2 and the rate of changing of carrier concentration and the rate of formation of these depletion regions are discussed exclusively in [19], [20], and [24].

To validate the model using experimental measurements, a clamped inductive switching test rig is used as shown in Fig. 1. As can be seen in Fig. 1, the low-side transistor is used to commutate the current away from the high-side free-wheeling diode, which in this case is the body diode of the MOSFET. The body diode of the MOSFETs under test is stressed by physically connecting the gate of the MOSFET to the source, thereby ensuring that the MOSFET never turns ON and current flows through the body diode in the reverse direction. By using the double pulse method, the low-side transistor is switched ON charging the inductor to a predefined current after which it is switched OFF thereby commutating the current to the body diode. When the low-side transistor is switched ON again, the high-side body diode goes into reverse recovery, which can trigger device destruction depending on the commutation rate, temperature, forward current density, etc. To validate the model, the results from the Fourier Series ADE (FS-ADE) solution are compared with experimental measurements on a discrete p-i-n diode as well as a finite-element device modeled using a simulator (Silvaco). A 1.2-kV/45-A IXYS p-i-n diode (DSI45-12a) coupled with a low-side transistor of suitable rating was tested. All the terminal voltages and currents were captured on a Tektronix oscilloscope. The semiconductor devices were placed in a thermal chamber where the ambient temperature was varied in order to analyze the temperature dependences of the switching transients [22], [23], [25], [26]. Fig. 2 shows the experiment setup including the test rig, chopper cell, the environmental chamber, and the oscilloscope used to carry out the measurements on the power devices.

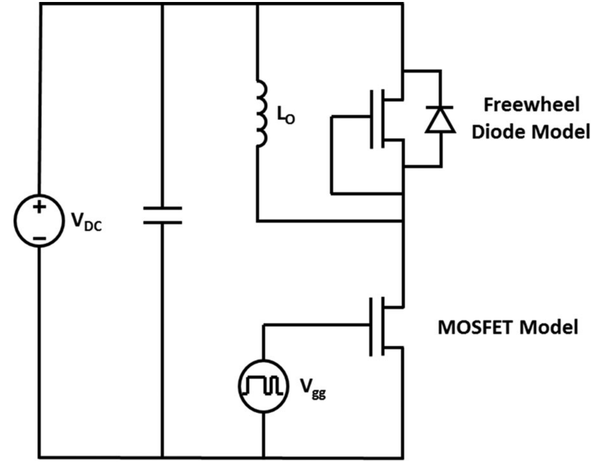

Fig. 1. Chopper cell circuit used to model the switching dynamics of body diode of a MOSFET and CoolMOS.

Fig. 2. Experimental setup. 1. The environmental chamber where the device temperature can be changed between −75 °C to 175 °C. 2. Function generator to produce double pulse. 3. Oscilloscope. 4. DC power supply for the gate drive and gate input signal. 5. DC link capacitors. 6. Inductive load. 7. Gate drive circuit.

Fig. 3(a) shows a comparison of the diode turn-off current for the experimental measurement, the FS-ADE model, and a finite-element simulation from Silvaco, while Fig. 3(b) shows a comparison of the voltage across the device during turn-off. Datasheet parameters were used together with known physical constants to obtain matching and the *dI/dt* of the current was varied by the gate resistance used to switch the low-side transistor. As can be seen from Fig. 3(a) and (b), the FS-ADE model is capable of replicating the current and voltage waveforms of

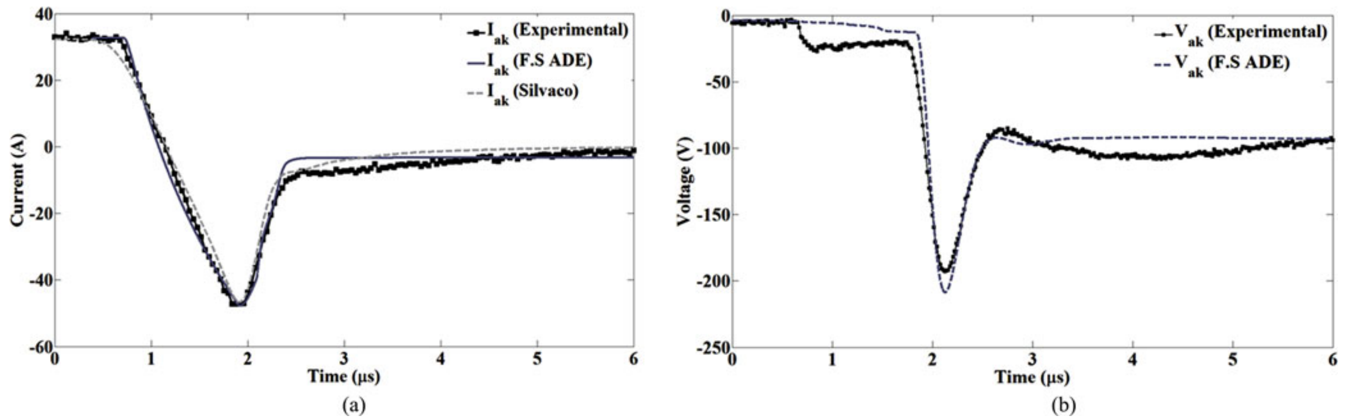

Fig. 3. Simulation validation: Diode reverse recovery (a) current waveform and (b) voltage waveform from the experimental results. Silvaco Finite Element device simulation and FS-ADE reconstruction simulation at the room temperature using 22 Ω gate resistance.

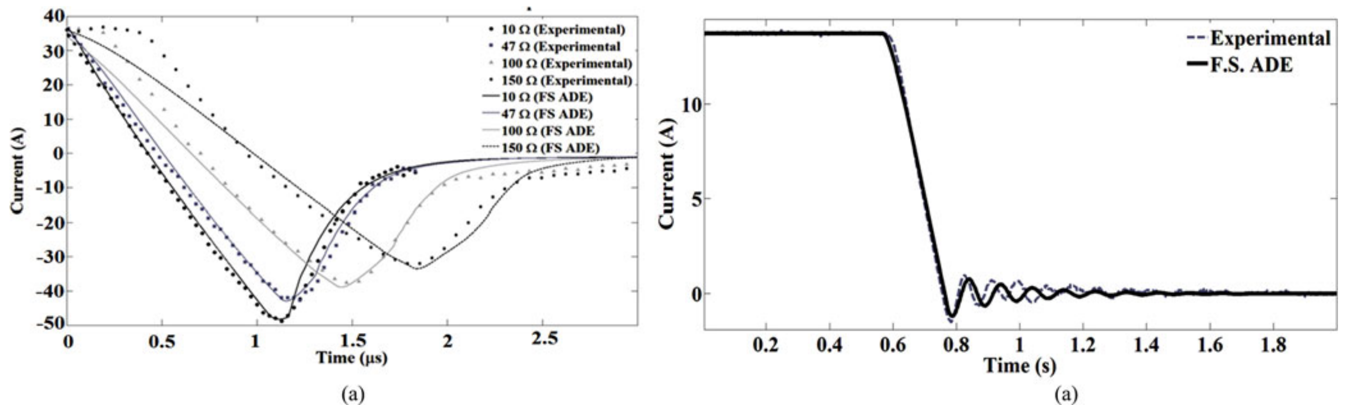

Fig. 4 (a). p-i-n diode reverse recovery waveform for different IGBT gate resistances (different *dI/dt*)—comparison between the experimental results and the simulation results using the FS-ADE reconstruction. (b). Measured and modeled reverse recovery characteristics of the SiC MOSFET body diode.

both the experimental measurements as well as finite-element models.

Fig. 4(a) shows the different reverse recovery waveforms of the discrete silicon p-i-n diode corresponding to different commutation rates modulated by the gate resistance of the low-side transistor. The reverse recovery characteristic of the body diode of a SiC MOSFET from Cree (C2M0160120D) is also modeled using the FS-ADE solution and validated by experimental measurements. Fig. 4(b) shows the results of the FS-ADE model together with the measurements of the reverse recovery characteristics of the SiC body diode. As can be seen in Fig. 4(a) and (b), there is good matching between the FS-ADE model and the experimental measurements. The material parameters were changed to match with the known material parameters of SiC, and the size of the device was changed accordingly using the existing data available on the device datasheet. Fig. 5(a) shows the measured reverse recovery characteristics of the CoolMOS body diode at different temperatures, whereas Fig. 5(b) shows that of the SiC MOSFET body diode at different temperatures. As can be seen from the experimental measurements in Fig. 5(b), there is very little reverse recovery charge in the SiC body diode compared with the CoolMOS body diode shown in Fig. 5(a) and the reverse characteristics of the SiC MOSFET body diode are temperature invariant. This is due to the very low minority carrier lifetime in SiC, which means that the stored charge in the drift region very quickly recombines during the turn-off of the body diode. Furthermore, the epitaxial voltage blocking drift layers in SiC are significantly thinner compared to that of silicon or CoolMOS; hence, there is less charge to be extracted during turn-off. The model developed for the silicon CoolMOS body diodes also takes the temperature dependence of the reverse recovery characteristics into account. As can be seen in Fig. 5(a), the CoolMOS device exhibits significant reverse recovery charge that increases with temperature due to increased carrier lifetime. For CoolMOS devices, modifications have been made to the Fourier solution of the ADE to account for the fact that it is not the conventional body diode, but rather alternate $\mathrm{PN^-N}$ and $\mathrm{PP^-N}$ diodes due to the superjunction architecture. Fig. 6(a) shows the structure of the conventional power MOSFET, while Fig. 6(b) shows the structure of a CoolMOS device with the $\mathrm{PP^-N}$ and $\mathrm{PN^-N}$ diodes along with the parasitic BJT, body resistance, and depletion capacitance. According to this structure, the device consists of a $\mathrm{PN^-N}$ and $\mathrm{PP^-N}$ diodes in parallel, due to the superjunction architecture, i.e., the minority carriers in the $\mathrm{PN^-N}$ diodes are holes while the minority carriers in the $\mathrm{PP^-N}$ diodes are

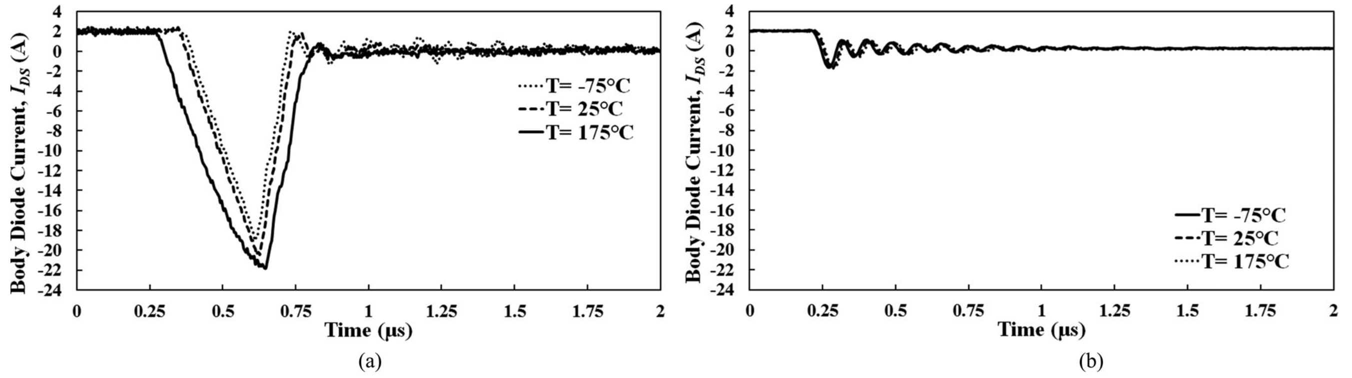

Fig. 5. (a) Measured reverse recovery current as a function of time for the CoolMOS body diode at different temperatures. (b) Measured reverse recovery current as a function of time for the SiC MOSFET body diode at different temperatures.

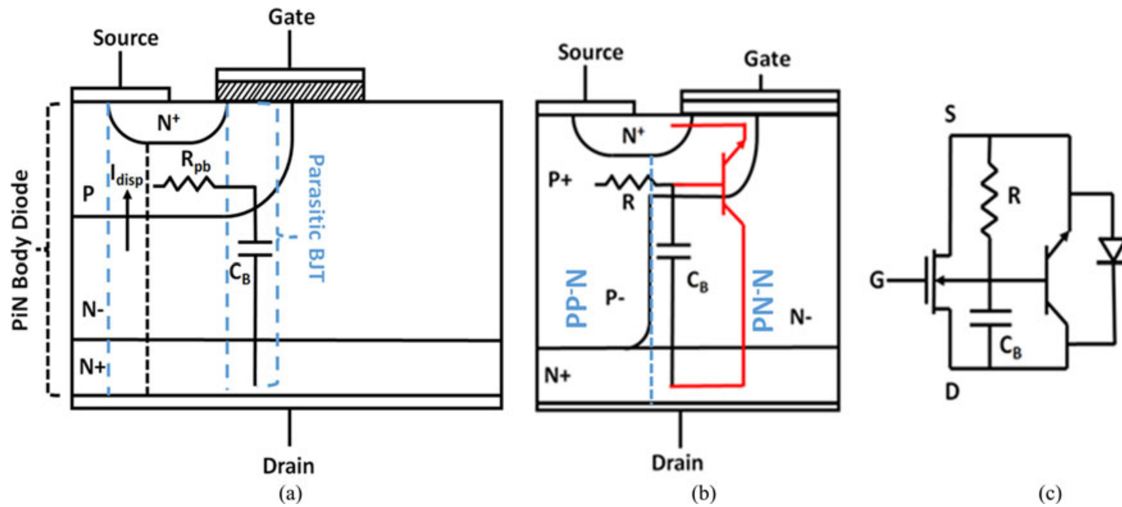

Fig. 6. (a) Vertical MOSFET structure. (b) CoolMOS structure including the parasitic BJT and a body diode. (c) Equivalent circuit of a MOSFET with the parasitic BJT and a body diode.

electrons. Consequently, the minority carrier lifetime and mobility of these carriers are different in the drift regions of the two different diodes. The electrons in the $\mathrm{PP^-N}$ diodes have a higher lifetime and larger diffusivity in comparison to holes in the $\mathrm{PN^-N}$ diodes. The model takes account of the larger charge stored in the body diode of a CoolMOS by utilizing these two parallel diodes. Basically, in order to model the $\mathrm{PP^-N}$ diode structure in the body diode of a CoolMOS, the n-type drift layer of a conventional p-i-n diode is replaced with a p-type material with a different background doping and the minority carriers are changed to electrons. This means that the diffusion coefficient (related to the mobility of carriers according to Einstein relationship for diffusion) and the carrier lifetime are changed (i.e., $\mu_n = 1330$ cm^2/V · s and $\mu_p = 450$ cm^2/V · s, τ_n (p type) $= 10$ μs and τ_p (n type) $= 1$ μs) [18], [19], [24], [27], [28]. Equation (8) is solved for $\mathrm{PN^-N}$ and $\mathrm{PP^-N}$ diodes keeping in mind that holes are the minority carriers in the former and electrons are the minority carriers in the latter. These modifications can account for a significantly higher reverse recovery charge in CoolMOS, which is necessary for modeling the body diode failure during the reverse recovery. The model is built in MATLAB Simulink and is solved using variable time steps. At the end of each time step, the carrier concentration in the drift region of the p-i-n diode, $p(x, t)$, is calculated using Fourier series reconstruction of the ADE in (8). Moreover, the boundary conditions of this equation are calculated at the end of each step and are fed back to the equation to be used in the next time step. The boundary conditions are the position of the depletion region at p-n$^-$ and n-n$^-$ junctions (x_1 and x_2, respectively) and the rate of change of the depletion width at these junctions (dp_1/dt and dp_2/dt). Using the data at each time step, the carrier concentration profile of the minority carriers in the drift region can be reconstructed and is shown in Fig. 6.

Fig. 7(a) shows the simulated minority carrier concentration profiles of the CoolMOS device $\mathrm{PP^-N}$ and $\mathrm{PN^-N}$ body diodes in the drift region, whereas Fig. 7(b) shows the minority carrier concentration profile of the SiC $\mathrm{PN^-N}$ body diode. The minority carrier profile in the plasma region of the devices is extracted right at the point before the devices are switched OFF from high-level injection mode during body diode conduction. As can be seen, the carrier concentration profile for $\mathrm{PP^-N}$ diode is higher than $\mathrm{PN^-N}$ diode, and hence, the reverse recovery waveform

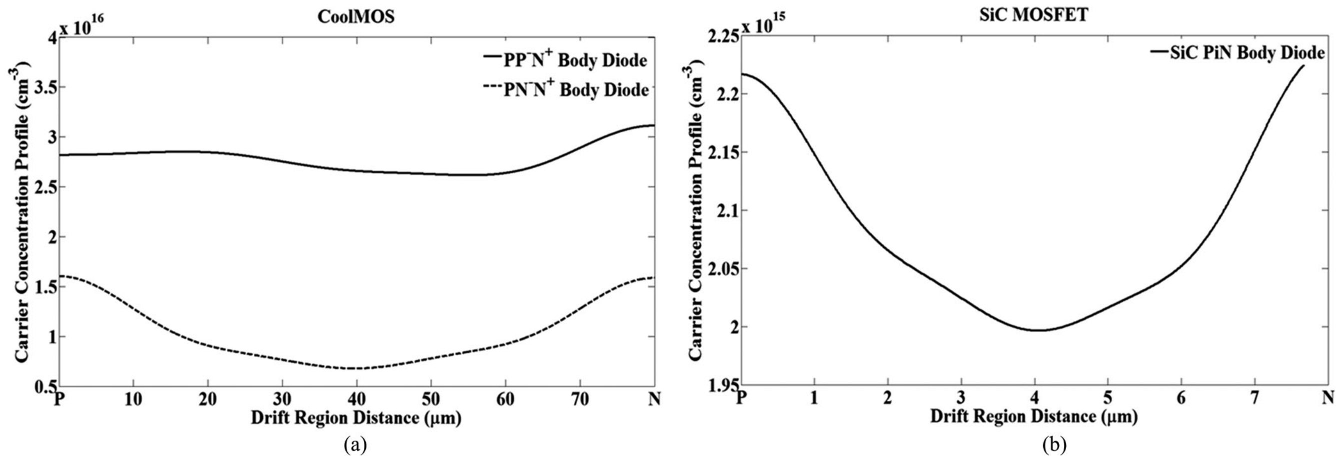

Fig. 7. (a) Carrier concentration profile in the drift region of a $\mathrm{PP^-N}$ and $\mathrm{PN^-N}$ body diodes of a CoolMOS and (b) the carrier concentration profile of a SiC MOSFET body diode during the high-level injection of these devices before switching off.

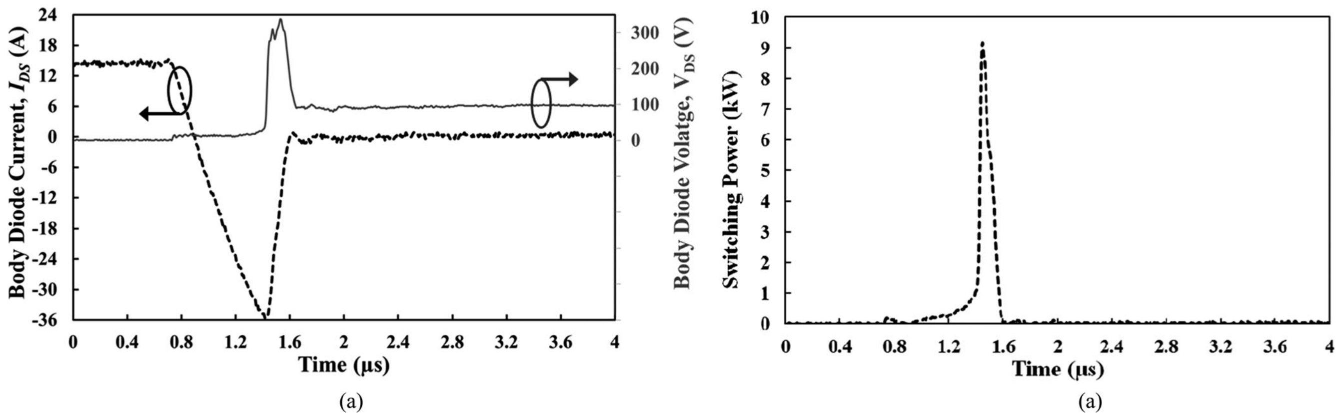

Fig. 8. (a) CoolMOS switching-off current and voltage waveform showing high *dI/dt* and *dV/dt* at the same instant of time. (b) Instantaneous switching power of CoolMOS during the switching off.

of CoolMOS is higher than a normal silicon or SiC-based p-i-n diode. This is confirmed by the experimental measurements on reverse recovery in the body diodes shown in Fig. 5(a) and (b). The higher minority carrier concentration in the $\mathrm{PP^-N}$ relative to the $\mathrm{PN^-N}$ diode is due to increased electron lifetime and higher electron diffusivity. Fig. 7(b) shows that the minority carrier concentration in the SiC p-i-n body diode is an order of magnitude lower than that in the CoolMOS.

III. BJT Electrothermal Model

The Fourier series solution to the ADE in p-i-n body diode has been used to explore the physics of MOSFET failure during the reverse recovery of the body diode. Fig. 6(a) shows a typical vertical MOSFET illustrating the antiparallel body diode and body resistance. Referring to Fig. 6(a), the p-well resistance is shown as R_{pb} and the drain-base capacitance is shown as C_B. The base current that triggers the BJT can come from the displacement current of the drain-to-body depletion capacitance during the body diode turn-off with high *dV/dt.* It can also be triggered by high *dV/dt* across the body diode during reverse recovery. As the reverse current reaches its peak, the depletion widths start to form across the junctions of the p-i-n diode and the remaining minority carriers in the drift region have to be recombined since carrier extraction is no longer possible. If the positive sloping recovery current (the recombination current between the peak reverse current and zero) is excessively high in the presence of parasitic inductance, large voltage overshoots coinciding with high peak reverse currents can cause very high instantaneous power dissipation across the device. This high instantaneous power causes high-temperature excursions that can trigger the parasitic BJT and destroy the device.

Fig. 8(a) shows the measured characteristics of a CoolMOS body diode in reverse recovery showing high reverse recovery current and simultaneously high peak voltage overshoot. Excessively snappy body diodes are known to be a reliability hazard under hard commutation [29]; hence, soft recovery diodes have been developed to mitigate this effect. The electrothermal modeling of the BJT, therefore, requires an accurate physics-based modeling of the diode's reverse recovery characteristics. To accurately model the electrothermal BJT, the displacement current of the drain-to-body capacitance as a function of *dV/dt* during

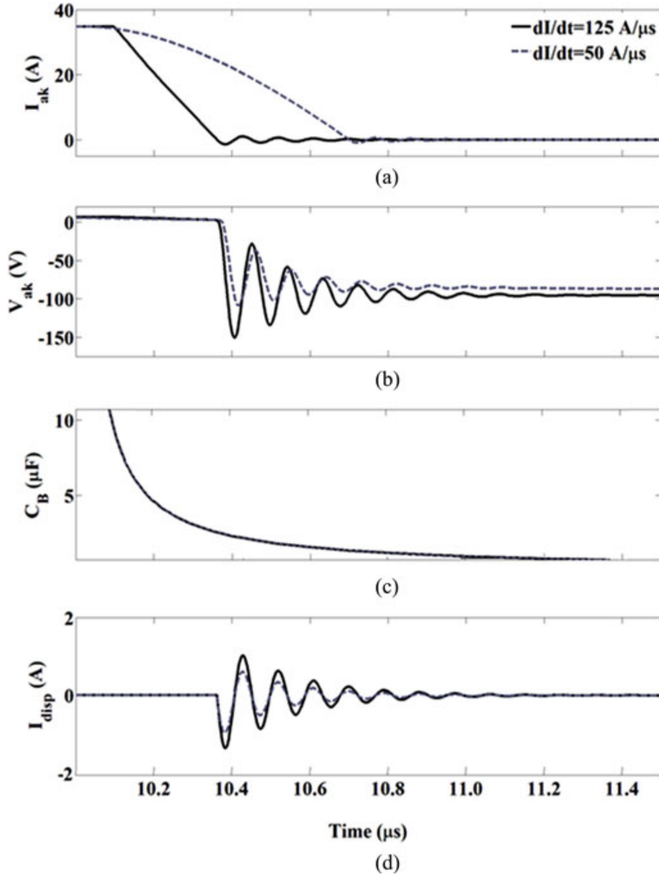

Fig. 9. FS-ADE simulation of the SiC MOSFET body diode displacement current, parasitic BJT base capacitance, and electric field at p^+n^- junction during turn-off.

turn-off must first be calculated. Fig. 9(a)–(d) shows the results of the FS-ADE simulations for two different switching rates (*dI/dt*). As the body diode is switched OFF, the low carrier lifetime in SiC results in a rapid extraction of the excess charge. The result of this is a fast rising voltage with a high *dV/dt* across the diode that is proportional to the switching rate. This can be seen in Fig. 9(b), where the overshoot is due to stray inductance (approximately between 100 and 200 nH). The peak overshoot increases with increasing *dI/dt*. As the diode begins to block, the electric fields at the junctions (p-n^- and n^-n^+) cause the depletion width to start extending into the drift region. The result is that the drain-body capacitance decreases and there is a resulting displacement current associated with the charging of the capacitance. Fig. 9(c) shows the simulated drain-base capacitance, whereas Fig. 9(d) shows the calculated displacement current. The depletion width (W_{d1}) and the drain-base capacitance (C_B) can be calculated using (9) and (10) as follows:

$$W_{d1} = -\frac{\varepsilon E_0}{q}\left(\frac{N_A + N_D}{N_A N_D}\right) \quad (9)$$

$$C_B = \frac{\varepsilon_i}{W_{d1}}. \quad (10)$$

In (9) and (10), NA (SiC: 2×10^{17} cm^{-3} and Si: 2×10^{19} cm^{-3}) and ND (SiC: 1.5×10^{15} cm^{-3} and Si: 1×10^{13} cm^{-3}) are the donor and acceptor doping of the p and n regions, respectively; q is unit electron charge; ε is the permittivity of SiC/Si (8.5845×10^{-13} F/cm and 1.05×10^{-12} F/cm respectively); and E_0 is the electric field at the metallurgical junction. As the depletion region widens, the base capacitance of the BJT decreases as shown in Fig. 9(c). The displacement current at the p-n^- junction can cause the parasitic BJT to latchup if there is sufficient body resistance to forward bias the parasitic BJT. This causes BJT latchup of the device by causing a voltage drop across the emitter–base junction of the BJT greater than the in-built voltage (φ_{BE}). The displacement current shown in Fig. 9(d) is calculated using (11). In this equation, A represents die area and a ratio between the cell size and the p-emitter of the body diode is considered as the die area of the body diode (SiC MOSFET die area is approximately 10.24 mm^2 and CoolMOS is approximately 20 mm^2, and the body diode ratio is assumed to be in the range of 10–20%). N_{eff} is the effective doping of the depletion region, and V_{CE} and V_{DS} are BJT's collector–emitter and MOSFET's drain–source voltages, respectively

$$I_{\mathrm{disp}} = \frac{\varepsilon A}{W} \cdot \frac{dV_{\mathrm{DS}}}{dt} = \left[\varepsilon A \sqrt{\frac{qN_{\mathrm{eff}}}{2\varepsilon V_{\mathrm{CE}}}}\right] \frac{dV_{\mathrm{DS}}}{dt}. \quad (11)$$

It can be seen from Fig. 9(d) that the peak displacement current increases with the switching rate. This means that faster switching devices are more likely to undergo parasitic BJT latchup. That displacement current flows through the body resistance (R_{pb}) of the MOSFET, which is the resistance between the p-body and the n-source. This p-body resistance (R_{pb}) can be calculated using (12), where L is the length of the base (0.9×10^{-4} cm), N_B is the base doping (2×10^{17} cm^{-3}), and A_B is the area of the base

$$R_{pb} = \frac{L}{q\mu_p N_B A_B}. \quad (12)$$

The mobility of holes (μ_p) in the base of the BJT is temperature dependent. Consequently, increasing the temperature reduces the hole mobility, hence increasing the base resistance. This increases the base–emitter voltage of the BJT. The temperature dependence of μ_p [30] is shown in (13). The critical MOSFET parameter that contributes to Avalanche breakdown is the body resistance, which must be minimized for a rugged MOSFET. In the equation below, index of i indicates holes or electrons. T is temperature of the device, N_{pg}, γ_p, α_p, and β_p depend on type of the material, and N is the dopant concentration

$$\mu_i = \mu_{i,\max} \frac{B_{i(N)}\left(\frac{T}{300}\right)\beta_i}{1 + B_{i(N)}\left(\frac{T}{300}\right)^{(\beta_i+\alpha_i)}} \quad (13)$$

$$B_{i(N)} = \left(\frac{\mu_{p,\max}}{\mu_{p,\max} - \mu_{p,\min}}\right) \frac{\left[1 + \left(\frac{N}{N_{pg}}\right)^{\gamma_p}\right]}{\left(\frac{N}{N_{pg}}\right)^{\gamma_p}} - 1 \Bigg|_{T=300\,\mathrm{K}}$$

$$\beta_p(\mathrm{4H-SiC}) = 0.5$$

$$\alpha_p(\mathrm{4H-SiC}) = 2.6$$

$$\gamma_p(\mathrm{4H-SiC}) = 0.5$$

$$\mu_{p,\max}(\mathrm{4H-SiC}) = 117\,\mathrm{cm}^2 \cdot \mathrm{V}^{-1} \cdot \mathrm{s}^{-1}$$

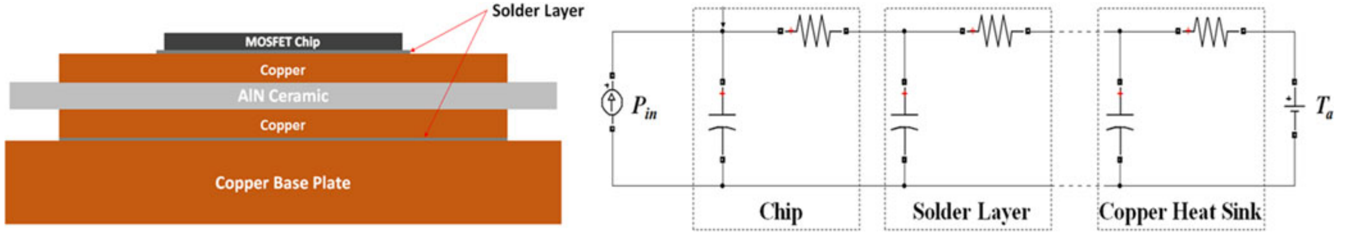

Fig. 10. Cross-sectional view of a basic hypothetical die mounted on top of a DBC and soldered to a base plate and the corresponding Cauer-network of this power module.

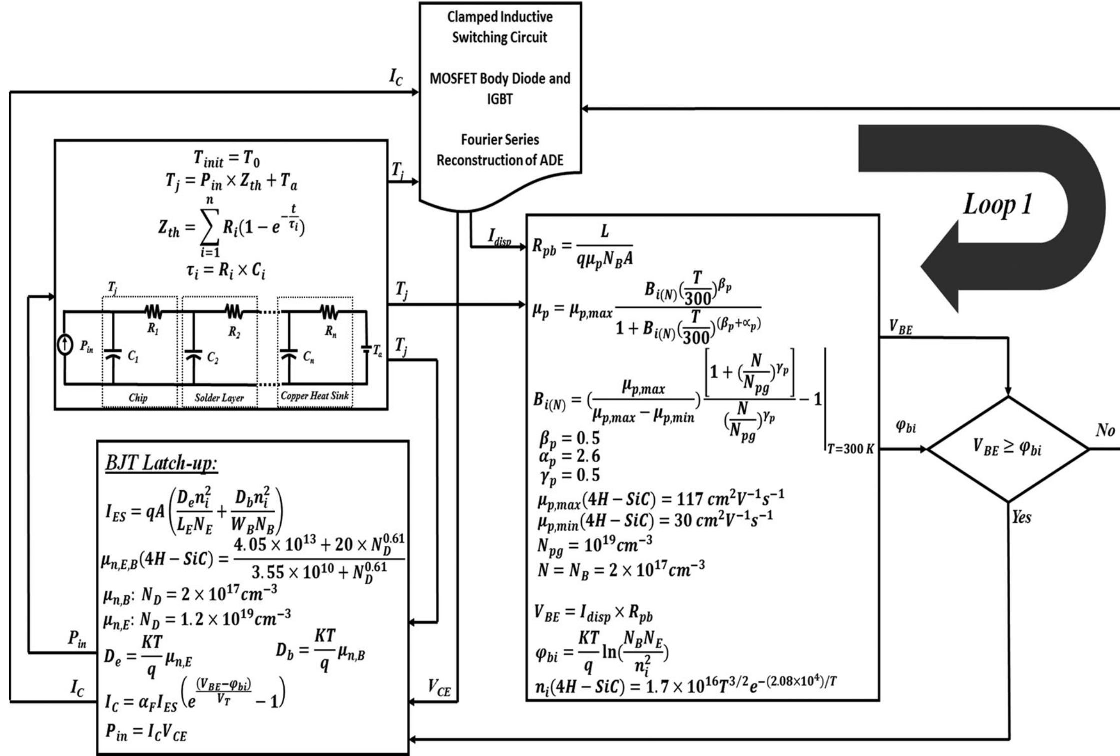

Fig. 11. Block diagram of the electrothermal parasitic BJT latchup coupled with the clamped inductive switching circuit model for a MOSFET body diode.

$$\mu_{p,\min}(4\mathrm{H-SiC}) = 30\,\mathrm{cm}^2 \cdot \mathrm{V}^{-1} \cdot \mathrm{s}^{-1}$$
$$N_{pg}(4\mathrm{H-SiC}) = 10^{19}\,\mathrm{cm}^{-3}$$
$$N = N_B = 2 \times 10^{17}\,\mathrm{cm}^{-3}.$$

By multiplying the body resistance in the displacement current induced by the p^+n^- junction of the p-i-n body diode, the base–emitter voltage (V_{BE}) of the BJT is calculated as

$$V_{\mathrm{BE}} = I_{\mathrm{disp}} \times R_{pb}. \tag{14}$$

The built-in voltage φ_{bi} of the parasitic BJT can be calculated using (15) as follows:

$$\varphi_{\mathrm{bi}} = \frac{KT}{q} \ln\left(\frac{N_B N_E}{n_i^2}\right) \tag{15}$$

where K is the Boltzmann constant, N_B and N_E ($1.2 \times 10^{19}\ \mathrm{cm}^{-3}$) are the base and emitter doping, respectively, and n_i is the intrinsic carrier concentration which is also temperature dependent and increases with temperature (T). Equation (16) shows this temperature dependence [17]

$$n_i(4\mathrm{H-SiC}) = 1.7 \times 10^{16} T^{3/2} e^{-(2.08\times 10^4)/T}. \tag{16}$$

If the voltage drop across the base-emitter of the BJT becomes greater than the built-in voltage of the parasitic BJT, then the BJT switches ON and a current starts flowing from the collector to the emitter of the BJT. In the proposed electrothermal model, the Ebers–Moll model is used to calculate the collector current. In the equation below, V_T is the thermal voltage. The applicability of Ebers–Moll model for large signal modeling is shown in [31]–[34]

$$I_C = \alpha_F I_{\mathrm{ES}} \left(e^{\frac{(V_{\mathrm{BE}} - \varphi_{\mathrm{bi}})}{V_T}} - 1\right) \tag{17}$$

$$I_{\mathrm{ES}} = qA\left(\frac{D_e n_i^2}{L_E N_E} + \frac{D_b n_i^2}{W_B N_B}\right) \tag{18}$$

where D_e and D_b are diffusion coefficients which are related to the electron mobility in the emitter and base of the parasitic BJT using Einstein relation (kinetic theory). L_E is emitter length, N_E is the emitter doping, and W_B is the base width of the BJT.

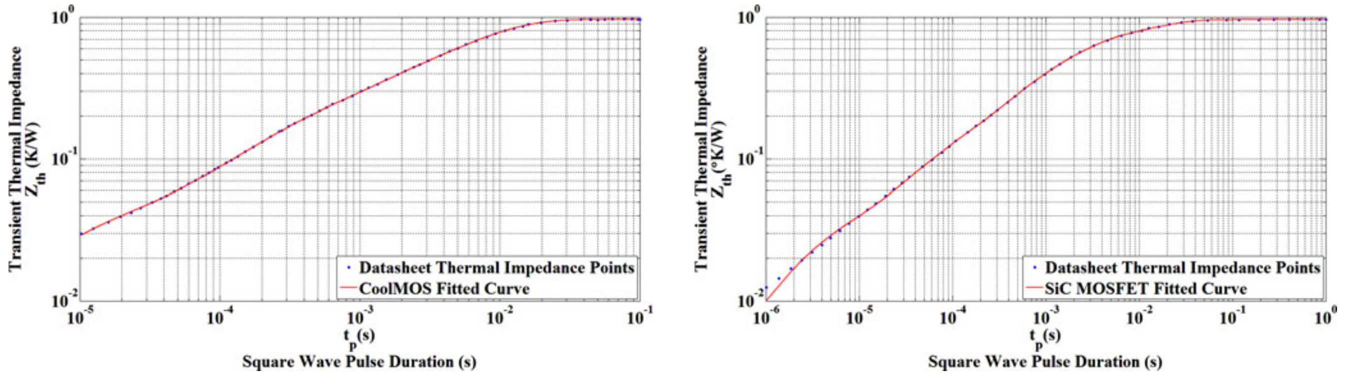

Fig. 12. Fitted curve of the transient thermal impedance of Infineon CoolMOS and Cree SiC MOSFET.

TABLE I
THERMAL RESISTANCE AND THERMAL CAPACITANCE FOR DEVICES CALCULATED FROM THE TRANSIENT THERMAL IMPEDANCE CURVE OF DEVICES

CoolMOS		SiC MOSFET	
$\mathbf{R_1}$	0.03867	$\mathbf{R_1}$	0.1164
$\mathbf{R_2}$	0.194	$\mathbf{R_2}$	0.08321
$\mathbf{R_3}$	0.3111	$\mathbf{R_3}$	0.2618
$\mathbf{R_4}$	0.4003	$\mathbf{R_4}$	0.2845
$\mathbf{R_5}$	0.02277	$\mathbf{R_5}$	0.2136
$\mathbf{C_1}$	1.99×10^{-4}	$\mathbf{C_1}$	3.3381×10^{-4}
$\mathbf{C_2}$	1.281×10^{-3}	$\mathbf{C_2}$	9.084×10^{-4}
$\mathbf{C_3}$	4.576×10^{-3}	$\mathbf{C_3}$	7.875×10^{-4}
$\mathbf{C_4}$	8.694×10^{-3}	$\mathbf{C_4}$	5.281×10^{-3}
$\mathbf{C_5}$	3.187×10^{-1}	$\mathbf{C_5}$	5.874×10^{-2}

The electron mobility can be calculated using (19) in which N_D is the donor doping

$$D_e = \frac{KT}{q}\mu_{n,E} \tag{19}$$

$$D_b = \frac{KT}{q}\mu_{n,B}$$

$$\mu_{n,E}(\mathrm{4H-SiC}) = \frac{4.05 \times 10^{13} + 20 \times N_D^{0.61}}{3.55 \times 10^{10} + N_D^{0.61}}$$

$$\mu_{n,B} : N_D = 2 \times 10^{17}\mathrm{cm}^{-3}$$

$$\mu_{n,E} : N_D = 2 \times 10^{19}\mathrm{cm}^{-3}.$$

As the BJT turns ON, the current passing through the device generates heat and the device temperature starts rising, which increases the base resistance and the body voltage. Consequently, the positive feedback loop increases the parasitic BJT forward current. This continues to generate more power until the temperature excursion due to the instantaneous power causes the device to break down. The calculated power is inserted into Cauer-network to model the junction temperature of the chip. Fig. 10 illustrates the cross-sectional view of a basic hypothetical power device mounted on top of a DBC and the equivalent Cauer-network of this power module. The flowchart of the model developed in Simulink is shown in Fig. 11. As can be seen in this figure, the temperature calculated from the thermal network [35] is fed back in a closed loop to recalculate the temperature dependent parameters in the clamped inductive circuit, base resistance, intrinsic carrier concentration, and the BJT base and collector currents. As can be seen in Fig. 11, if the BJT does not latchup, then the current continues to flow in the body diode until it reaches zero and the simulation model works in *Loop1* shown in the figure. The values of thermal resistors and capacitors for the Cauer-network are calculated by taking these steps:

Step 1: Finite sample points from the transient thermal impedance curve (junction to case) obtained from a single pulse power input of the power device were captured from the device datasheet (Cree SiC MOSFET and Infineon CoolMOS CE technology).

Step 2: Using curve fitting tool in MATLAB, a rational fitting method is used to reconstruct the curve (see Fig. 12). Here, the Cauer-network impedance equation is considered to be the base of curve fitting as it can give physical meaning to each layer; however, the Foster network may be used as well. Each parameter in the curve fitting tool is set to have an upper and lower limits based on the geometry, specific heat capacity, density, and thermal conductance of the material to achieve reasonable values for thermal resistance and thermal capacitance of the Cauer-network thermal chain. Note that based on the Cauer-network impedance equation, the numerator degree is one order smaller than the denominator degree. It is critical for this study to have an accurate curve fitting within the μs level as the transient occurs in μs. Consequently, the fifth-order Cauer network is considered for both SiC MOSFET and CoolMOS which in case of TO-247 may be interpreted as the die, solder layer, adhesive layer, the copper base plate, CTE-matched high flow EMC (epoxy molding compound) packaging. Equation (20) shows the reconstruction of the thermal impedance using rational curve fitting for the device:

$$Z_{\mathrm{th}} = \frac{p_1 s^4 + p_2 s^3 + p_3 s^2 + p_4 s + p_5}{s^5 + q_1 s^4 + q_2 s^3 + q_3 s^2 + q_4 s^1 + q_5}. \tag{20}$$

Step 3: The impedance from the junction to case of a Cauer-network can be calculated using the following equation:

$$z'_{\mathrm{th}} = \cfrac{1}{C_1 s + \cfrac{1}{R_1 + \cfrac{1}{\cdots + \cfrac{1}{C_i s + \cfrac{1}{R_i}}}}}. \tag{21}$$

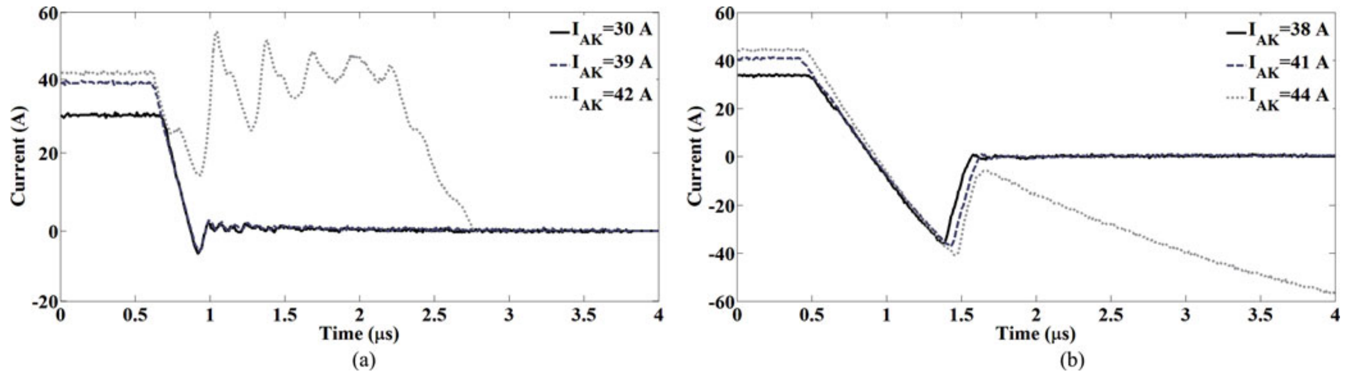

Fig. 13. (a) Experimental results showing SiC MOSFET body diode reverse recovery at varied forward currents. (b) Experimental results showing CoolMOS body diode reverse recovery at varied forward current.

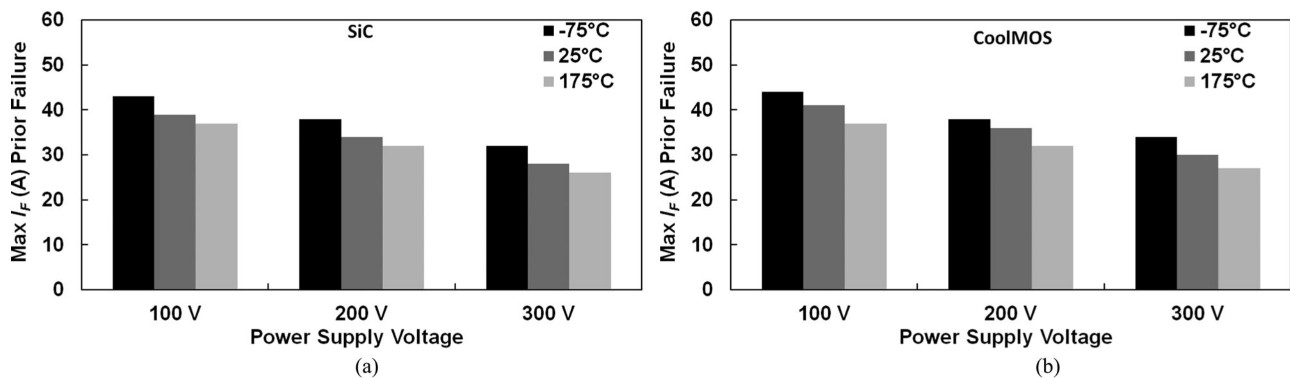

Fig. 14. (a) Parasitic BJT latchup current at different temperatures (SiC MOSFET). (b) Parasitic BJT latchup at different temperatures (CoolMOS).

Step 4: Since the denominator of (20) is one order higher than the numerator, by calculating the admittance of (20), the value of C_1 can be calculated. By inverting the remainder of this calculation, the impedance of the remainder can be calculated, which will result in the value of R_1. By continuing this process, R_1, R_2, C_1, and C_2 are calculated. Table I shows the calculated values for SiC MOSFET and CoolMOS devices. The differences between the thermal parameters of the CoolMOS and SiC Power MOSFET arise from the difference in die sizes primarily. As a result of the wide bandgap and higher critical electric field, the SiC MOSFET is a smaller die compared to the CoolMOS; hence, it has a higher thermal resistance and a smaller thermal capacitance. The model with the Fourier series method of reconstructing the charge storage region is described in [28] and [36], where the parameters are defined and techniques for extracting the values for these parameters are described in detail. The values for parameters come directly from measurements and datasheets information. The parameters for the electrothermal model and parasitic BJT are obtained from the measurements and datasheet information and by comparing the simulation waveforms with the experimental results.

IV. Results and Discussion

Using the clamped inductive switching circuit, two different failure modes were captured on the oscilloscope. The devices under test were a Si-based super-junction MOSFET (P/N: 726-IPW90R340C3) from Infineon and a Cree SiC power MOSFET (P/N: C2M0160120D). The gate and source of the MOSFETs were clamped and their body diodes were used as freewheeling diodes in the clamped inductive switching test rig. By increasing the first pulse duration during the inductor charging phase of the double pulse test, different forward currents were passed through the body diodes and the waveforms were captured. This current was increased until the device failed. The maximum forward current that triggers a fail during turn-off is defined as the latching current for each technology. Fig. 13(a) shows the reverse recovery current waveform of the SiC MOSFET body diode at different forward currents. SiC MOSFET has a very small carrier lifetime in the intrinsic region in comparison to Si-based devices, and consequently, the reverse recovery of these devices is significantly smaller than conventional devices. As can be seen, the device failed at 42-A forward current as the parasitic BJT latched up. Fig. 13(b) illustrates the reverse recovery waveform obtained from the CoolMOS device body diode during the reverse recovery. As can be seen, by increasing the forward current density, the reverse recovery increases as a result of higher stored charge which is unlike the silicon carbide MOSFET where the reverse recovery current of the body diode was independent of the forward current. At the forward current of 44 A, there is a sufficient rise in the junction temperature to cause failure in the device. It can also be noticed

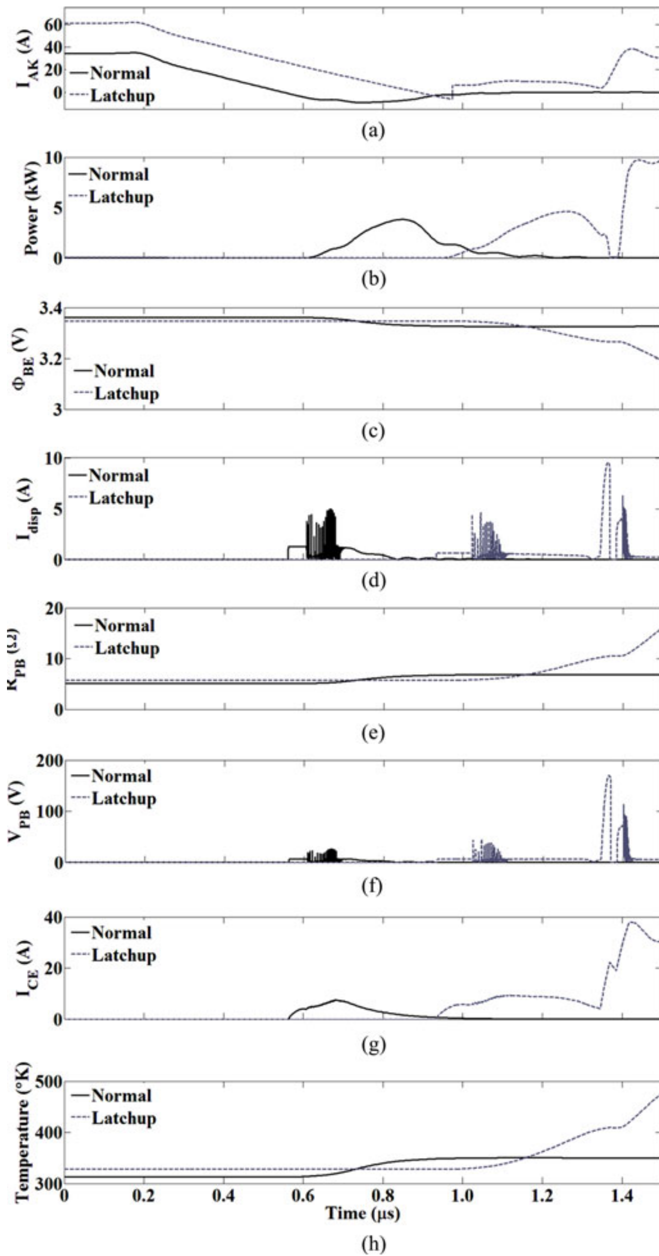

Fig. 15. Parasitic BJT transient electrothermal behavior.

that the CoolMOS device typically fails during reverse recovery, whereas the SiC device fails during the turn-off transient and that the *dI/dt* of the SiC body diode is higher than that of the CoolMOS. The impact of temperature and the supply voltage on the latching current was investigated for the SiC and CoolMOS devices. The temperature was varied from −75 to 175 °C and the supply voltage was also varied from 100 to 300 V. Similar to the previous measurements, the forward current was increased until the device failed during reverse recovery of the body diode. Fig. 14(a) shows the parasitic latchup current for SiC MOSFET at different temperatures, while Fig. 14(b) shows the same graph for CoolMOS power MOSFET. As the supply voltage and temperature are increased, the latching current for device failure decreases as is expected because both voltage and temperature contribute to BJT latchup. As explained earlier, if the parasitic BJT latches up, the device might fail. There are different parameters that cause the parasitic BJT to latch up during the reverse recovery of the body diode such as high *dV/dt*, high current density, and high temperature. Using the introduced electrothermal model for the parasitic BJT, the impact of increasing the current density and temperature on the SiC MOSFET and CoolMOS body diode can be investigated. Fig. 15 shows how the electrothermal BJT latchup model of the SiC MOSFET behaves under normal condition when there is no thermal runaway (normal), as well as when the device undergoes thermal runaway (latchup). The condition that triggers thermal runaway in this case is a higher forward current. As can be seen from Fig. 15, as the body diode undergoes the switching transient in (a) for two different forward currents, the instantaneous power dissipated across the diode shown in (b) causes a temperature rise. The instantaneous power dissipation increases with the forward current. This temperature rise causes the in-built junction voltage ($\Phi_{\rm BE}$) to fall as shown in Fig. 15(c). It can be seen from Fig. 15(c), that the device with the higher forward current experiences a higher drop in $\Phi_{\rm BE}$ due to higher dissipated power. The fall in $\Phi_{\rm BE}$ is a result of increased carrier concentration from bandgap narrowing as shown in (15). Fig. 15(d) shows the displacement current ($I_{\rm disp}$) caused by the charging of the drain-body depletion capacitance and the impact of the dissipated power on the p-body resistance ($R_{\rm PB}$) is shown in Fig. 15(e). The rise in $R_{\rm PB}$ is due to the increasing temperature calculated from the thermal network and caused by the power dissipated during the turn-off of the body diode. It can be seen that the device with the higher forward current has a higher rise in $R_{\rm PB}$. Fig. 15(f) shows the body voltage ($V_{\rm PB}$) which is $I_{\rm disp} \times R_{\rm PB}$ and acts as the base-to-emitter voltage of the parasitic BJT. At the point where VPB becomes greater than $\Phi_{\rm BE}$, the parasitic BJT turns ON and produces a collector-to-emitter current ($I_{\rm CE}$) calculated from the Ebers–Moll model in (17). Fig. 15(g) shows the calculated $I_{\rm CE}$ for the two parasitic BJTs where the device with the higher forward current can be seen to exhibit a more rapid increase in $I_{\rm CE}$ with no corresponding decrease. It can also be seen from Fig. 15(g) that although the device with the smaller forward current has a parasitic BJT that turns ON, however, the temperature rise is such that it does not allow the positive electrothermal feedback process to set in. Fig. 15(h) shows the respective temperature plots for each device. The model developed in Fig. 15 has been used to simulate the behavior of the device under three different forward currents. The results are shown in Fig. 16 for the SiC MOSFETs and Fig. 17 for the CoolMOS MOSFETs. Figs. 16 and 17 explain the experimental observations of Figs. 13 and 14 using the developed model. As can be seen from the results of the model, the predicted rise in temperature and the on-set of thermal runaway occurs at higher forward currents for both technologies. The model correctly predicts that the higher forward current causes higher instantaneous power dissipation as well as higher body diode reverse recovery charge (in the case of the CoolMOS) which triggers thermal runaway as a result of BJT latchup. Fig. 16(a) shows the SiC MOSFET body diode turn-off characteristics at different forward currents, whereas

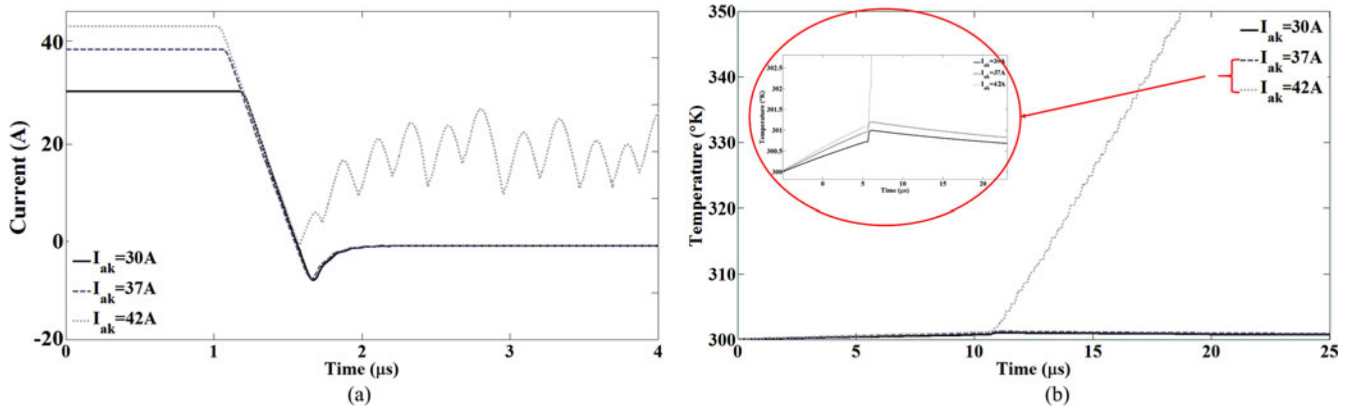

Fig. 16. (a) Simulation results showing reverse recovery waveform of SiC MOSFET body diode for varied forward current. (b) Temperature rise within the device during the body diode reverse recovery.

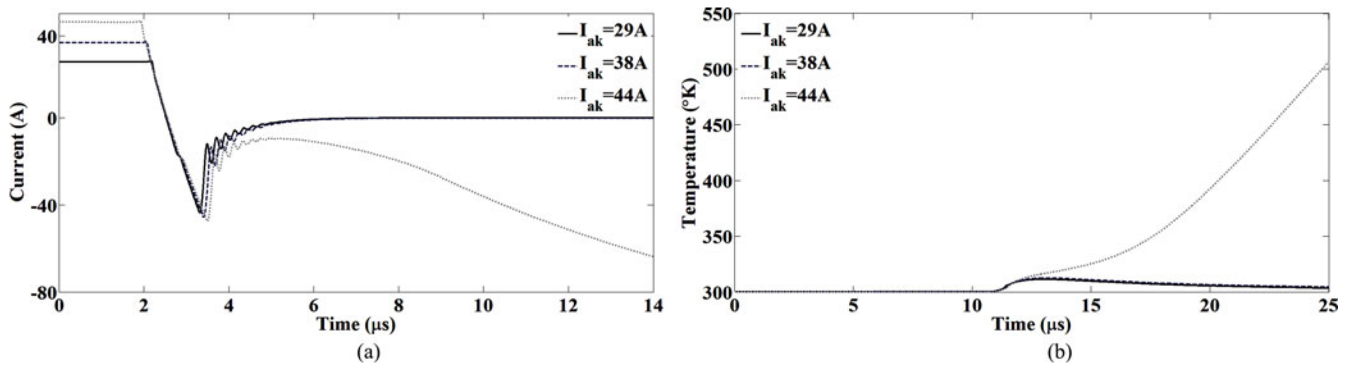

Fig. 17. (a) Simulation results showing reverse recovery waveform of CoolMOS body diode for varied forward current. (b) Temperature rise within the device during the body diode reverse recovery.

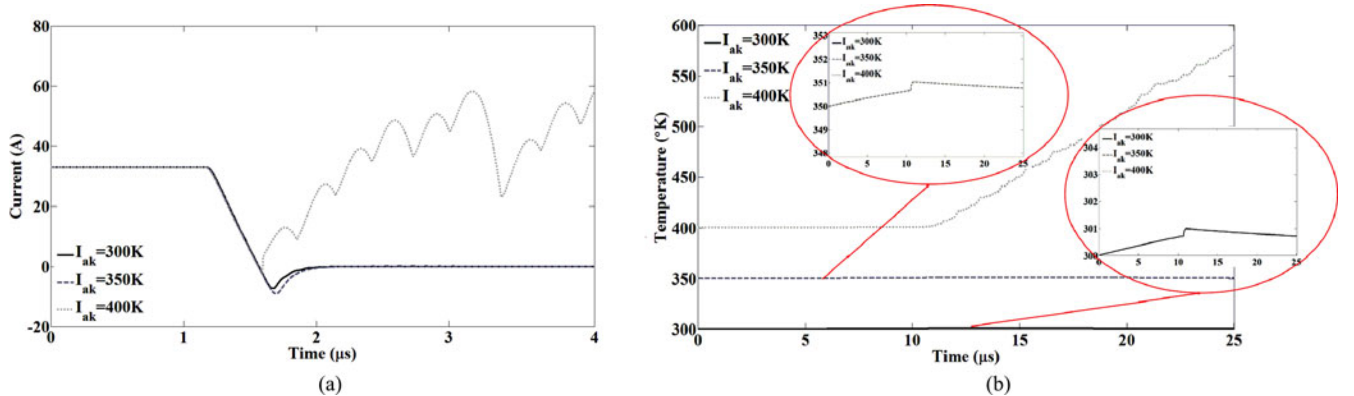

Fig. 18. (a) Simulation results showing reverse recovery waveform of SiC body diode for varied temperature. (b) Temperature rise within the device during the body diode reverse recovery.

Fig. 16(b) shows the calculated temperature from the flowchart shown in Fig. 11. For the normal operation mode, the temperature rise was approximately estimated to rise around 1 °C and 1.5 °C for the normal operation of the devices at 33 and 42 A, respectively in the single switching event. This small temperature rise is due to the small reverse recovery of SiC MOSFET and small energy dissipation within the device for a single switching event. Fig. 17(a) and (b) shows similar plots for the CoolMOS device where it can be seen that the model is capable of predicting BJT latchup at higher forward current densities. The model

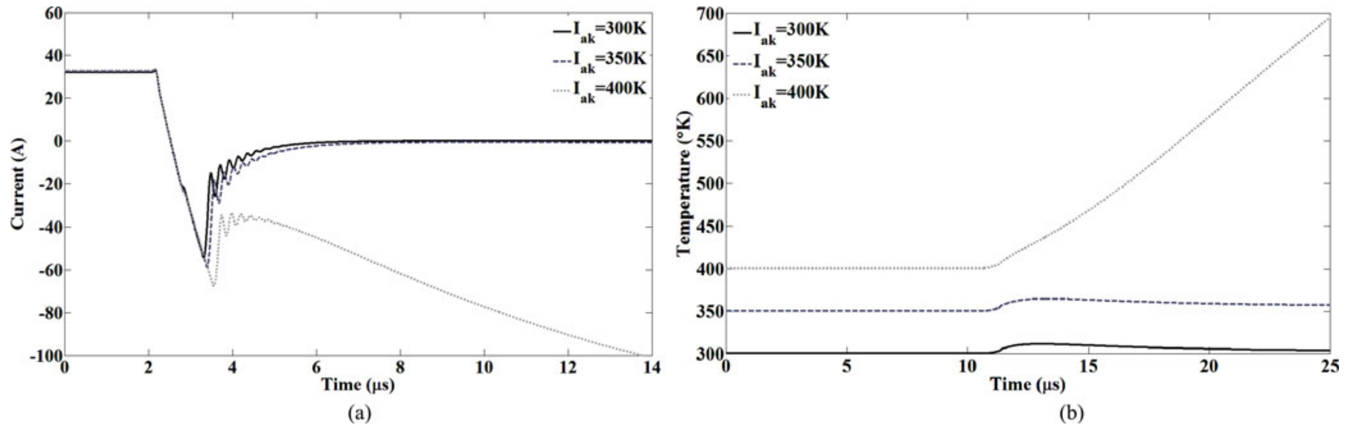

Fig. 19. (a) Simulation results showing reverse recovery waveform of CoolMOS body diode for varied temperature. (b) Temperature rise within the device during the body diode reverse recovery.

can also be used to accurately predict the impact of temperature on the thermal runaway during reverse recovery. Simulations have, therefore, been performed at different ambient temperatures to investigate how well the model predicts latchup at different temperatures. At higher temperature, the mobility of the hole is reduced, and consequently, the p-body resistance increases. This brings about higher base–emitter voltage and causes the parasitic BJT's high current. Fig. 18(a) shows the body diode turn-off current characteristics for the SiC MOSFET at three different temperatures (25 °C, 75 °C, and 125 °C). As can be seen, the device fails at 125 °C due to thermal runaway. The calculated temperature is shown in Fig. 18(b) for the SiC MOSFET where it can be seen that thermal runaway results in an uncontrollable rise in temperature. Fig. 19(a) shows the body diode current turn-off characteristics for the CoolMOS device at different temperatures similar to Fig. 18(a) for the SiC MOSFET. Fig. 19(b) shows the simulated temperature of the CoolMOS device corresponding to Fig. 19(a). On comparing Figs. 19(b) and 18(b), it can be seen that the rate of temperature rise for the SiC MOSFET is larger than the CoolMOS. This is due to smaller thermal capacitance of the SiC die in comparison to the CoolMOS. The differences between the SiC MOSFET and the CoolMOS device arise from the difference between the thermal resistances (which is dependent on the die size), the semiconductor material, and the device architecture. The SiC MOSFET is able to sustain a significantly larger avalanche current density in spite of having a higher thermal resistance. This is due to the wide bandgap which makes the device more temperature resilient. The SiC device fails during turn-off before the zero crossing of the current because of the combination of high *dV/dt* and the drain-to-body depletion capacitance generating a displacement current which flows through the body resistance and triggers the parasitic BJT. The high thermal resistance of the MOSFET coupled with the temperature sensitive body resistance means that the device can fail during turn-off as a result of high ambient temperature, high forward current density, and higher commutation rates. In case of the CoolMOS device, the excessive reverse recovery charge causes high instantaneous power dissipation which raises the temperature of the device and triggers the parasitic BJT. Hence, the device fails in reverse recovery after the zero crossing as opposed to the SiC MOSFET where the failure is before the zero crossing.

V. Conclusion

This paper has introduced a computationally efficient and accurate compact model that can be used to predict and diagnose electrothermal bipolar latchup in power MOSFETs. The model was used to investigate the reliability of SiC MOSFET and superjunction MOSFET body diodes during reverse recovery. SiC Cree MOSFETs and Infineon CoolMOS were tested in a clamped inductive switching test rig and the body diode of the upper switch was used as a free-wheeling diode. Moreover, the SiC MOSFET p-i-n body diode and CoolMOS were modeled using the Fourier series reconstruction of the ADE to calculate the excessive carrier stored in the drift region during the switching transition. In the case of the CoolMOS device, the ADE was modified to account for the fact that electrons will also be minority carriers in the p-pillars of the drift region. An electrothermal model of the BJT was developed alongside of the clamped inductive switching circuit to simulate the thermal runaway of these devices under the reverse recovery. The thermal resistance and capacitance for the packaged devices from Cree and Infineon were calculated and used in the Cauer thermal network. Moreover, the temperature of the device at each step of the simulation was fed back to the device and all the temperature-dependent parameters were calculated after each step. The reverse recovery of the model was validated by comparing the results with the experiments. Experiments show that thermal runaway is exacerbated by high current densities and temperatures, which is well predicted and replicated by the model.

References

[1] C. Xu, L. Xing-Ming, J. K. O. Sin, and K. Bao-wei, "Improving the CoolMS^{TM} body-diode switching performance with integrated Schottky contacts," in *Proc. IEEE 15th Int. Symp. Power Semicond. Devices ICs*, 2003, pp. 304–307.

[2] T. Funaki, M. Matsushita, M. Sasagawa, T. Kimoto, and T. Hikihara, "A study on SiC devices in synchronous rectification of DC-DC converter," in *Proc. 22nd Annu. IEEE Appl. Power Electron. Conf.*, 2007, pp. 339–344.

[3] D. De, A. Castellazzi, A. Solomon, A. Trentin, M. Minami, and T. Hikihara, "An all SiC MOSFET high performance PV converter cell," in *Proc. 15th Eur. Conf. Power Electron Appl.*, 2013, pp. 1–10.

[4] C. D. Brown and B. Sarlioglu, "Reducing switching losses in BLDC motor drives by reducing body diode conduction of MOSFETs," in *Proc. IEEE Energy Convers. Congr. Expo.*, 2013, pp. 4286–4293.

[5] S. Buonomo, S. Musumeci, R. Pagano, C. Porto, A. Raciti, and R. Scollo, "Driving a new monolithic cascode device in a DC–DC converter application," *IEEE Trans. Ind. Electron.*, vol. 55, no. 6, pp. 2439–2449, Jun. 2008.

[6] J. Jordan, V. Esteve, E. Sanchis-Kilders, E. J. Dede, E. Maset, J. B. Ejea, and A. Ferreres, "A comparative performance study of a 1200 V Si and SiC MOSFET intrinsic diode on an induction heating inverter," *IEEE Trans. Power Electron.*, vol. 29, no. 5, pp. 2550–2562, May 2014.

[7] Z. Jun, C. F. Wheatley, R. Stokes, C. Kocon, and S. Benczkowski, "Optimization of the body-diode of power MOSFETs for high efficiency synchronous rectification," in *12th Int Symp. Power Semicond. Devices ICs*, 2000, pp. 145–148.

[8] R. Siemieniec, O. Blank, M. Hutzler, L. J. Yip, and J. Sanchez, "Robustness of MOSFET devices under hard commutation of the body diode," in *Proc. 15th Eur. Conf. Power Electron. Appl.*, 2013, pp. 1–10.

[9] Y. Shaoyong, A. Bryant, P. Mawby, X. Dawei, L. Ran, and P. Tavner, "An industry-based survey of reliability in power electronic converters," *IEEE Trans. Ind. Appl.*, vol. 47, no. 3, pp. 1441–1451, May/Jun. 2011.

[10] Z. Hui and L. M. Tolbert, "Efficiency impact of silicon carbide power electronics for modern wind turbine full scale frequency converter," *IEEE Trans. Ind. Electron.*, vol. 58, no. 1, pp. 21–28, Jan. 2011.

[11] G. Busatto, G. V. Persiano, and F. Iannuzzo, "Experimental and numerical investigation on MOSFET's failure during reverse recovery of its internal diode," *IEEE Trans. Electron Devices*, vol. 46, no. 6, pp. 1268–1273, Jun. 1999.

[12] F. Iannuzzo, G. V. Persiano, and G. Busatto, "Measurement of the BJT activation current during the reverse recovery of power MOSFET's drain-source diode," *IEEE Trans. Electron Devices*, vol. 48, no. 2, pp. 391–393, Feb. 2001.

[13] A. Bryant, "Simulation and optimisation of diode and IGBT interaction in a chopper cell," Doctoral dissertation, Queens' College, University of Cambridge, Cambridge, U.K., 2005.

[14] G. M. Buiatti, F. Cappelluti, and G. Ghione, "Power PiN diode model for PSpice simulations," in *Proc. 20th Annu. IEEE Appl Power Electron. Conf. Expo.*, 2005, vol. 3, pp. 1911–1916.

[15] A. T. Bryant, G. J. Roberts, A. Walker, and P. A. Mawby, "Fast inverter loss simulation and silicon carbide device evaluation for hybrid electric vehicle drives," in *Proc. Power Convers. Conf.*, 2007, pp. 1017–1024.

[16] P. A. Mawby, P. M. Igic, and M. S. Towers, "Physically based compact device models for circuit modelling applications," *Microelectron. J.*, vol. 32, pp. 433–447, May 2001.

[17] B. J. Baliga, *Fundamentals of Power Semiconductor Devices*. New York, NY, USA: Springer, 2008.

[18] L. Lu, A. Bryant, E. Santi, J. L. Hudgins, and P. R. Palmer, "Physical modeling and parameter extraction procedure for p-i-n diodes with lifetime control," in *Proc. IAS Annu. Meeting. Conf. Record IEEE Ind. Appl. Conf.*, 2006, pp. 1450–1456.

[19] A. T. Bryant, P. R. Palmer, E. Santi, and J. L. Hudgins, "A compact diode model for the simulation of fast power diodes including the effects of avalanche and carrier lifetime zoning," in *Proc. IEEE 36th Power Electron. Spec. Conf.*, 2005, pp. 2042–2048.

[20] A. T. Bryant, L. Liqing, E. Santi, P. R. Palmer, and J. L. Hudgins, "Physical modeling of fast p-i-n diodes with carrier lifetime zoning, part I: Device model," *IEEE Trans. Power Electron.*, vol. 23, no. 1, pp. 189–197, Jan. 2008.

[21] P. A. Mawby, A. T. Bryant, P. R. Palmer, E. Santi, and J. L. Hudgins, "High speed electro-thermal models for inverter simulations," in *Proc. 25th Int. Conf. Microelectron.*, 2006, pp. 166–173.

[22] P. M. Igic, P. A. Mawby, M. S. Towers, and S. Batcup, "Dynamic electro-thermal physically based compact models of the power devices for device and circuit simulations," in *Proc. 17th Annu. IEEE Symp. Semicond. Thermal Meas. Manage.*, 2001, pp. 35–42.

[23] A. Bryant, N. A. Parker-Allotey, D. Hamilton, I. Swan, P. A. Mawby, T. Ueta, T. Nishijima, and K. Hamada, "A fast loss and temperature simulation method for power converters, Part I: Electrothermal modeling and validation," *IEEE Trans. Power Electron.*, vol. 27, no. 1, pp. 248–257, Jan. 2012.

[24] A. T. Bryant, P. R. Palmer, E. Santi, and J. L. Hudgins, "Simulation and optimization of diode and insulated gate bipolar transistor interaction in a chopper cell using MATLAB and Simulink," *IEEE Trans. Ind. Appl.*, vol. 43, no. 4, pp. 874–883, Jul./Aug. 2007.

[25] Z. Zhou, M. S. Khanniche, P. Igic, S. T. Kong, M. Towers, and P. A. Mawby, "A fast power loss calculation method for long real time thermal simulation of IGBT modules for a three-phase inverter system," Proc.presented at the 2005 Eur. Conf. Power Electron. Appl., Dresden, Germany, 2005.

[26] A. N. Githiari, B. M. Gordon, R. A. McMahon, L. Zhong-Min, and P. A. Mawby, "A comparison of IGBT models for use in circuit design," *IEEE Trans. Power Electron.*, vol. 14, no. 4, pp. 607–614, Jul. 1999.

[27] T. Gachovska, J. L. Hudgins, A. Bryant, E. Santi, H. A. Mantooth, and A. K. Agarwal, "Modeling, Simulation, and Validation of a Power SiC BJT," *IEEE Trans. Power Electron.*, vol. 27, no. 10, pp. 4338–4346, Oct. 2012.

[28] A. T. Bryant, K. Xiaosong, E. Santi, P. R. Palmer, and J. L. Hudgins, "Two-step parameter extraction procedure with formal optimization for physics-based circuit simulator IGBT and p-i-n diode models," *IEEE Trans. Power Electron.*, vol. 21, no. 2, pp. 295–309, Mar. 2006.

[29] Z. Xi, J. Lei, D. Junjun, L. Siqi, and C. Zheng, "Analysis and design of a new soft-switching boost converter with a coupled inductor," *IEEE Trans. Power Electron.*, vol. 29, no. 8, pp. 4270–4277, Aug. 2014.

[30] T. T. Mnatsakanov, L. I. Pomortseva, and S. N. Yurkov, "Semiempirical model of carrier mobility in silicon carbide for analyzing its dependence on temperature and doping level," *Semiconductors*, vol. 35, pp. 394–397, 2001/04/01 2001.

[31] I. E. Getreu, *Modeling the Bipolar Transistor*. Amsterdam, The Netherlands: Elsevier, 1978.

[32] R. L. Bailey, "Large-signal nonlinear analysis of a high-power high-frequency junction transistor," *IEEE Trans. Electron Devices*, vol. ED-17, no. 2, pp. 108–119, Feb. 1970.

[33] C. D. Root, J. Melillo, and S. Sammon, "Computer modeling of diode forward recovery characteristics," *IEEE Trans. Electron Devices*, vol. ED-29, no. 3, pp. 461–463, Mar. 1982.

[34] T. Shih-Wei, C. Hon-Rung, C. Wei-Tien, H. Meng-Kai, L. An-Hung, and W. Lour, "Characterization and modeling of three-terminal heterojunction phototransistors using an InGaP layer for passivation," *IEEE Trans. Electron Devices*, vol. 52, no. 2, pp. 204–210, Feb. 2005.

[35] A. Merkert, T. Krone, and A. Mertens, "Characterization and scalable modeling of power semiconductors for optimized design of traction inverters with Si- and SiC-devices," *IEEE Trans. Power Electron.*, vol. 29, no. 5, pp. 2238–2245, May 2014.

[36] A. T. Bryant, P. R. Palmer, J. L. Hudgins, E. Santi, and X. Kang, "The use of a formal optimisation procedure in automatic parameter extraction of power semiconductor devices," in *Proc. IEEE 34th Annu. Power Electron. Spec. Conf.*, 2003, vol. 2, pp. 822–827.

Roozbeh Bonyadi (S'14) received the B.Sc. (1st class hons.) degree in electrical and electronics engineering from the Shahed University of Tehran, Tehran, Iran, and the M.Sc. degree (with a Merit) in electronic systems from the University of Warwick, Coventry, U.K. His M.Sc. project was intelligent fault diagnosis in automotive electronic systems of systems of premium vehicles in collaboration with Jaguar Land Rover PLC.

He then started working as a KTP Associate at the University of Wolverhampton in collaboration with Phoenix Calibration & Services Ltd. His interest in hybrid/electric vehicles and semiconductor devices and power module packaging led him to undertake a Ph.D. in power electronics at the University of Warwick. His Ph.D. project is sponsored by the EPSRC in collaboration with Jaguar Land Rover and involves design, simulation, implementation, and packaging of automotive power inverters.

Mr. Bonyadi is a Member of the IEEE Industry Applications Society and the IEEE Power Electronics Society.

Olayiwola Alatise (M'05) received the B.Eng. degree (with first-class honors) in electronic engineering and the Ph.D. degree in microelectronics and semiconductors from Newcastle University, Newcastle upon Tyne, U.K., in 2008.

His research is focused on mixed-signal performance enhancements in strained Si/SiGe metal–oxide–semiconductor field-effect transistors (MOSFETs). In June 2008, he joined the Innovation R&D Department, NXP Semiconductors, as a Development Engineer, where he designed, processed, and qualified discrete power trench MOSFETs for automotive applications and switched-mode power supplies. In November 2010, he became a Science City Research Fellow with the University of Warwick, Coventry, U.K., where since August 2012, he has been an Assistant Professor of electrical engineering. His research interests include investigating advanced power semiconductor materials and devices for improved energy conversion efficiency.

Saeed Jahdi (S'10) received the B.Sc. degree in electrical power engineering from the University of Science and Technology, Tehran, Iran, in 2005, and the M.Sc. degree (with distinction) in power systems and energy management from City University London, London, U.K., in 2012. Since then, he has been working toward the Ph.D. degree in electrical engineering at the Power Electronics Laboratory, School of Engineering, University of Warwick, Coventry, U.K.; he has been awarded an energy theme scholarship for the duration of his research.

His current research interests include wide bandgap semiconductor devices in high-voltage power converters, circuits, and applications. He is currently working on silicon-carbide-based solid-state fault current limiters, with collaboration with Western Power Distribution, U.K.

Mr. Jahdi is a Member of the IEEE Power Electronics Society and the IEEE Industrial Electronics Society.

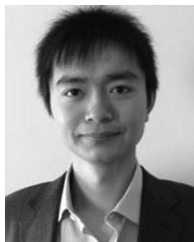

Ji Hu (S'15) received the B.Sc. degree in electronic and electrical engineering from Northumbria University, Newcastle upon Tyne, U.K., in 2011, and the M.Sc. degree in energy and power electronics from the University of Warwick, Coventry, U.K., in 2013, where he is currently working towards the Ph.D. degree in power electronics. His research interest is on the reliability of high voltage SiC power devices and finite-element device simulations.

Jose Angel Ortiz Gonzalez received the degree in electrical engineering from the University of Vigo, Vigo, Spain, in 2009.

From 2010 to 2012, he was a Support Technician at the Department of Electronics Technology, University of Vigo. Since 2013, he has been with the School of Engineering, University of Warwick, Coventry, U.K., as a Senior Power Electronics Research Technician, currently focusing on high-voltage silicon-carbide-based dc–dc and dc–ac power converters. His current research interests include power converters, circuit testing, and device evaluation.

Li Ran (M'98–SM'07) received the Ph.D. degree in power systems engineering from Chongqing University, Chongqing, China, in 1989.

He was a Research Associate with the Universities of Aberdeen, Nottingham, and Heriot-Watt, at Aberdeen, Nottingham, and Edinburgh in the U.K., respectively. He became a Lecturer in power electronics with Northumbria University, Newcastle upon Tyne, U.K., in 1999 and was seconded to Alstom Power Conversion, Kidsgrove, U.K., in 2001. Between 2003 and 2012, he was with Durham University, U.K. He joined the University of Warwick, Coventry, U.K. as a Professor in Power Electronics and Systems in 2012. His research interests include the application of power electronics for electric power generation, delivery, and utilization.

Philip A. Mawby (S'85–M'86–SM'01) received the B.Sc. and Ph.D. degrees in electronic and electrical engineering from the University of Leeds, Leeds, U.K., in 1983 and 1987, respectively. His Ph.D. was focused on GaAs/AlGaAs heterojunction bipolar transistors for high-power radio frequency applications at the GEC Hirst Research Centre, Wembley, U.K.

In 2005, he joined the University of Warwick, Coventry, U.K., as the Chair of power electronics. He was also with the University of Wales, Swansea, U.K., for 19 years and held the Royal Academy of Engineering Chair for power electronics, where he established the Power Electronics Design Center. He has been internationally recognized in the area of power electronics and power device research. He was also involved in the development of device simulation algorithms, as well as optoelectronic and quantum-based device structures. He has authored or coauthored more than 100 journal and conference papers. His current research interests include materials for new power devices, modeling of power devices, and circuits.

Prof. Mawby has been involved in many international conference committees, including the ISPSD, EPE, and the ESSDERC. He is a Chartered Engineer, a Fellow of the IET, and a Fellow of the Institute Physics. He is a Distinguished Lecturer for the IEEE Electron Devices Society.